Intermodel spread of East Asian summer monsoon simulations in CMIP5

Jinqiang Chen[1] and Simona Bordoni[1]

[1]Environmental Science and Engineering, California Institute of Technology, Pasadena, California, USA

Abstract In this paper we diagnose the intermodel spread in the Coupled Model Intercomparison Project Phase 5 (CMIP5) East Asian summer monsoon (EASM) simulations in the context of the moist static energy and moisture budgets. We find that the spatial distribution of the EASM precipitation simulated by different models is highly correlated with the meridional stationary eddy velocity, defined as the deviation from the long-term zonal mean. The correlation becomes more robust when energy fluxes into the atmospheric column are considered, consistent with recent observational analyses. The spread in the area-averaged rainfall amount can be partially explained by the spread in the simulated globally averaged precipitation, with the rest primarily due to the lower level meridional wind convergence. Clear relationships between precipitation and zonal and meridional eddy velocities are observed.

1. Introduction

The East Asian summer monsoon (EASM) constitutes an important branch of the Asian monsoon system and is primarily associated with its prominent quasi-stationary Meiyu-Baiu (MB) rainfall band, which brings summer rains to densely populated areas in East Asia. The dynamics of the EASM has long been investigated because of its importance in sustaining rapidly growing economies and possible implications for the paleohistories of the monsoon and the Tibetan Plateau (TP) on geological timescales. Additionally, a better understanding of the MB might provide insights into other Subtropical Convergence Zones (STCZs) sharing similar features [*Kodama*, 1992].

State-of-the-art global climate models (GCMs) participating in the World Climate Research Programme Coupled Model Intercomparison Project Phase 3 (CMIP3) and Phase 5 (CMIP5) have been shown to grossly capture the large-scale pattern of the EASM precipitation, but wide across model spread exists [*Huang et al.*, 2013; *Sperber et al.*, 2012; *Song et al.*, 2013; *Song and Zhou*, 2013]. While CMIP5 models have a slightly enhanced skill relative to CMIP3 in simulating the EASM climatological precipitation in terms of multi-model mean (MMM) [*Sperber et al.*, 2012], significant biases in MMM rainfall amounts and spatial distribution remain. Fundamental issues related to the representation of basic physical processes in GCMs, such as moist convection [*Bony et al.*, 2013; *Huang et al.*, 2013; *Stevens and Bony*, 2013; *Chen et al.*, 2010] and large-scale circulations [e.g., *Ceppi et al.*, 2012; *Huang et al.*, 2013], have been argued to be limiting factors in improved climate simulations, together with relatively coarse resolution, especially in regions with complicated topography like Asia [e.g., *Boos and Hurley*, 2013].

Previous studies on the EASM have emphasized the role of the subtropical westerly jet and the lower level poleward flow around the western Pacific subtropical high in the formation of the MB system [e.g., *Kodama*, 1992; *Sampe and Xie*, 2010; *Chen and Bordoni*, 2014], but the exact mechanisms by which such flows respond to the large-scale and local forcing and interact with the EASM precipitation remain debated. In a recent study, for example, *Chen and Bordoni* [2014] (hereafter, CB14) investigated the moist static energy (MSE) budget of the MB system using observations and numerical simulations. They found that both zonal and meridional advection of atmospheric moist enthalpy, and primarily of dry enthalpy, as opposed to latent energy, sustains the rainfall band in a region of otherwise negative net energy input into the atmospheric column. The moisture budget, directly relating the net precipitation to the moisture flux convergence, was also examined to better quantify the contribution to the rainfall intensity by evaporation and circulation. Finally, numerical simulations with and without the TP allowed us to explore how the presence of the TP modifies the MSE and moisture budgets and hence influences the EASM.

In this study, we use the understanding we have developed on the dynamics of the EASM based on the MSE and moisture budgets to expose parameters that explain the biases in precipitation amounts and spatial structure in the CMIP5 EASM simulations. In return, the different present-day EASM simulations confirm the robustness of our theoretical framework in climate models. While not directly translatable into recommendations for model improvements, our results identify processes that are central for better constraining model simulations and projections of the EASM.

2. Data and Methods

In this study, we examine the CMIP5 decadal2000 hindcasts. The decadal predictions in CMIP5 consist of a series of 10 year or 30 year forecasts with initial observed climate states and take into account both the long-term mean forced response and the internal decadal variability [*Meehl et al.*, 2009; *Taylor et al.*, 2012]. Here decadal2000 predictions are composed of 10 year integrations, initialized at the end of year 2000, in which ocean initial conditions are representative of either the observed anomaly or full fields for the start date (i.e., full-field and anomaly initialization methods), but land, sea ice, and atmosphere initial conditions are chosen at the discretion of different modeling groups [*Taylor et al.*, 2012]. Historical runs differ from decadal runs in that they are started from stochastically selected preindustrial states, and the synchronization between climate predictions and internal variability is not guaranteed. Especially when multiensemble mean techniques are used to increase the predicability of long-term simulations (e.g., historical runs) in each individual model, the internal variability is suppressed and only an estimate of the forced response survives [*Meehl et al.*, 2007]. We prefer the decadal2000 run to the historical and Representative Concentration Pathways (RCP) runs, as they allow for a better comparison with observations.

Monthly data of decadal2000 integrations from 2001 to 2009 from 17 coupled climate models and three additional simulations with different initialization methods (a total of 20 experiments; refer to the legend of Figure 2) are used to assess the model performance. All available ensembles for each individual model are averaged. When computing the MSE and moisture budgets as described below, we first average monthly fields over June and July, then compute all budget terms, and finally produce a long-term climatology by averaging over the nine available years. We also present results in which the long-term climatology (9 year average) is applied before computing individual budget terms. The difference between the two climatologies lies in that the former (latter) includes (neglects) interannual transient eddies. While the mature MB phase is traditionally considered to span from June 15 to July 14, here we average over both June and July, because most model outputs are available on monthly averages. Accordingly, we focus on the broader EASM region (Figure 1a, enclosed regions), which includes East China (20°–42°N, 110°–122°E, including the Meiyu region) and the Changma-Baiu-northwestern-Pacific (CBP, 122°–170°E, with an upper latitudinal bound of 42°N, and a lower latitudinal bound linearly varying with longitude from 20°N to 30°N). In the context of the MSE budget (equation (1)), vertical pressure velocity is used as a proxy for precipitation. This is a good approximation in continental deep convection regions, such as the Meiyu region, but might be less satisfactory in the CBP region, where precipitation is a mixture of deep convection and large-scale condensation along isentropes associated with extratropical storms [CB14, *Sampe and Xie*, 2010]. For this reason, in addition to results for the overall large-scale EASM domain, we also separately discuss East China and the CBP region.

Monthly observed precipitation is obtained from GPCP (Global Precipitation Climatology Project) and TRMM (Tropical Rainfall Measuring Mission) provided from Observations for Model Intercomparison Projects (obs4MIPs) (http://obs4mips.llnl.gov:8080/wiki/ [*Teixeira et al.*, 2011]) project hosted on the Earth System Grid Federation (http://esgf.org). Wind field, temperature, and humidity are obtained from European Centre for Medium-Range Weather Forecasts (ECMWF) Re-Analysis (ERA) Interim (37 pressure levels, 512 × 256 N128 Gaussian grid, analysis fields produced for 0000, 0600, 1200, and 1800 UTC) in the Data Support Section of the National Center for Atmospheric Research (NCAR), while precipitation, surface heat fluxes, and radiation are obtained from the ERA-Interim (1.5° grid [*Dee et al.*, 2011]) 3 h forecast fields produced from forecasts beginning at 0000 and 1200 UTC. All data from model forecasts and observations are bilinearly interpolated to a 1° × 1° grid, if necessary. Since there are systematic differences over ocean and land between GPCP and TRMM [*Adler et al.*, 2000], both data sets are used here as observational references (Figures 1b and 1c). We also use the ERA-Interim precipitation to assess consistency and robustness between climate models and the European Centre for Medium-Range Weather Forecasts operational forecasting model.
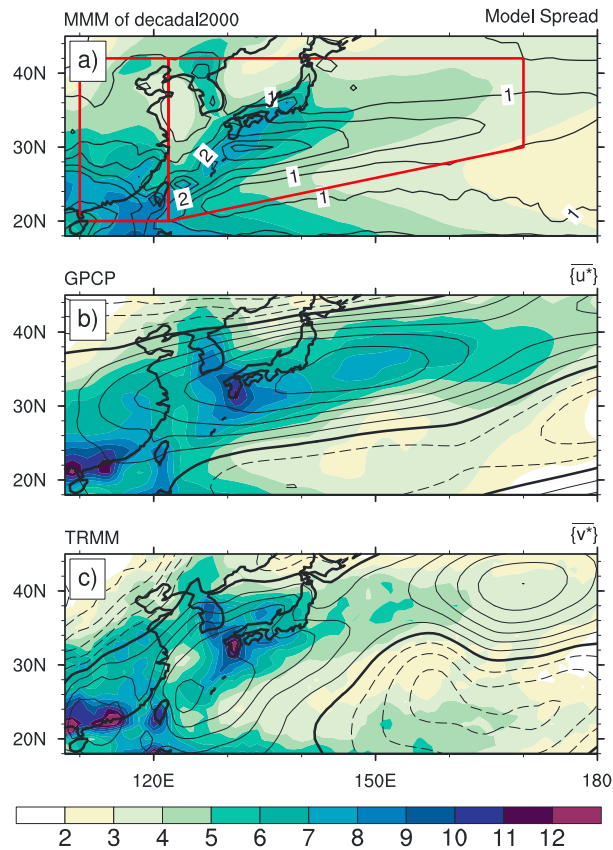
Figure 1. June and July climatological mean precipitation (shaded, mm d^{-1}) for the 2001–2009 9 year period for the CMIP5 decadal2000 (a) MMM, (b) GPCP, and (c) TRMM. Line contours (contour interval 0.5 mm d^{-1}) in Figure 1a show the model spread or standard deviation of the 20 experiments listed in Figure 2. Line contours in Figures 1b and 1c show vertically normalized stationary zonal and meridional eddy velocities, $\{\overline{u^*}\}$ and $\{\overline{v^*}\}$ (contour interval 1 m s^{-1} and 0.4 m s^{-1}), respectively. Red lines enclose the EASM region, comprising East China and the CBP region. See text for details.

Following CB14, we use the MSE and moisture budgets to interpret the intermodel spread of the EASM in the decadal2000 predictions. As a review, the MSE budget over a climatological period is

$$\langle \overline{w\partial_p h} \rangle = \overline{F^{net}} - \langle \overline{\mathbf{v} \cdot \nabla E} \rangle, \tag{1}$$

where $h = C_p T + gz + L_v q$ is the MSE; $E = C_p T + L_v q$ is the atmospheric moist enthalpy; $\overline{F^{net}}$ is the net energy flux into the atmosphere and is given by the sum of net radiative fluxes at the surface and top of atmosphere, and surface sensible heat and latent heat fluxes; $\mathbf{v}$ is the horizontal wind field (u, v); w is vertical velocity; and $\langle \cdot \rangle$ indicates the mass-weighted vertical integral $\int (\cdot) dp/g$. To the extent that the MSE stratification $\partial_p h$ remains everywhere negative, equation (1) links upward motion to regions of positive $\overline{F^{net}} - \langle \overline{\mathbf{v} \cdot \nabla E} \rangle$. We further decompose each field into mean, stationary eddy, and transient eddy components, where conventionally $(\cdot)'$ indicates the deviation from the time mean $\overline{(\cdot)}$ (here the two month June and July mean for each individual year), i.e., $u' = u - \overline{u}$, and $(\cdot)^*$ denotes the deviation from the global zonal mean $[\cdot]$, i.e., $u^* = u - [u]$. By performing a similar decomposition using reanalysis data, CB14 found that two stationary eddy fluxes, $-\langle [\overline{u}]\overline{\partial_x T^*} \rangle$ and $-\langle \overline{v^*[\partial_y T]} \rangle$, are the major contributors to the horizontal moist enthalpy advection. The first term, $-\langle [\overline{u}]\overline{\partial_x T^*} \rangle$, represents the advection by the mean zonal flow of zonal temperature asymmetries, due to anomalous heating by the TP, convection, and land-sea thermal contrast [*Sampe and Xie*, 2010]. The second term, $-\langle \overline{v^*[\partial_y T]} \rangle$, is the advection of the mean meridional temperature gradient by the stationary eddy velocity and can be further approximated as proportional to $\langle \overline{v^*} \rangle$ at any given latitude, given that $[\overline{\partial_y T}]$ is almost height independent in the free troposphere (Figure 11d in CB14). Physically, positive stationary meridional eddy velocity $\langle \overline{v^*} \rangle$, arising from zonal asymmetries, transports warm air from the south to the EASM region. Given their role in determining the spatial pattern of positive upward motion, and hence precipitation, in the EASM region, $\overline{F^{net}}$, $-\langle [\overline{u}]\overline{\partial_x T^*} \rangle$, $-\langle \overline{v^*[\partial_y T]} \rangle$, and $\langle \overline{v^*} \rangle$ will be used to assess the model performance in simulating the spatial structure of the EASM rainfall.

The intermodel spread in rainfall amounts is investigated using the moisture budget:

$$\overline{P} - \overline{E} = -\langle \overline{\nabla \cdot \mathbf{v}q} \rangle, \tag{2}$$

which, over a climatological average, directly relates the net precipitation $\overline{P - E}$ to the horizontal moisture flux convergence $-\langle \overline{\nabla \cdot \mathbf{v}q} \rangle$. This term is further decomposed into contributions by the wind convergence $-\langle \overline{q\nabla \cdot \mathbf{v}} \rangle$ and moisture advection $-\langle \overline{\mathbf{v} \cdot \nabla q} \rangle$.

3. Assessment of Intermodel Spread

Global MSE and moisture budgets between June and July are evaluated across all climate models and ERA-Interim. All models satisfy the global moisture budget by which $[\overline{P}] \approx [\overline{E}]$, with the exception of Flexible Global Ocean-Atmosphere-Land System model, spectral version 2 (FGOALS-s2), in which $[\overline{E}] \sim 3.2$ mm d^{-1} and $[\overline{P}] \sim 2.7$ mm d^{-1}. Over the climatological June and July average, the global precipitation is not strictly energetically constrained [e.g., *O'Gorman et al.*, 2012], because of coupling between solar insolation and hemispheric asymmetries in heat capacity. In boreal summer, the atmosphere gains energy, resulting in a positive heat storage in all climate models, mostly ranging from 0.5 W m^{-2} to 3.0 W m^{-2}, and with a maximum of 7.0 W m^{-2} in CFSv2-2011. ERA-Interim is known to have unbalanced moisture and MSE budgets [*Berrisford et al.*, 2011]. Hence, while we analyze and discuss results based on all models and observed data, we exclude FGOALs-s2, ERA-Interim, and observations from our regression analysis.

The climatological MMM captures reasonably well the elongated band of the EASM precipitation spanning from East Asia into the northwest Pacific, but precipitation amounts are underestimated compared to both GPCP and TRMM (Figure 1), due to biases in both precipitation intensity and spatial extent. Precipitation is particularly underestimated over the EASM oceanic region compared to GPCP, with better agreement with TRMM. The systematic bias between TRMM and GPCP found here, with lower TRMM estimates over EASM oceanic regions, is consistent with previous studies [*Adler et al.*, 2009]. The intermodel spread (Figure 1a) is large in both heavily precipitating continental regions and mildly precipitating oceanic regions. The large spread in the former might be accounted for by different convective parameterizations and simulated circulations [e.g., *Song and Zhou*, 2013; *Zhou et al.*, 2009] in different models, with discrepant simulations of high precipitation generating large standard deviations. The large spread in the latter appears to be more related to differences in the simulated spatial structure of precipitation over the northwestern Pacific. The analyses below allow for a more in depth understanding of the intermodel spread in both spatial structure and precipitation amounts in the EASM region.

3.1. Spatial Structure

Figure 2 shows the spatial centered pattern correlations between precipitation and the MSE budget terms identified in CB14 as fundamental in determining the spatial patterns of upward motion. A relatively high correlation between precipitation and $\overline{F^{\text{net}}}$ is observed and agreed upon amongst climate models, particularly in the CBP region. This is not unexpected given that $\overline{F^{\text{net}}}$ depends on the circulation itself and, through changes in energy and radiative fluxes because of clouds, is influenced by model-dependent physical parameterizations of clouds, radiation, and air-sea interaction. The observed TRMM and GPCP rainfall estimates have relatively low correlation with the ERA-Interim $\overline{F^{\text{net}}}$.

From a large-scale perspective, the subtropical westerly jet advects warm air from the TP to the MB region and induces ascending motion through $-\langle [\overline{u}] \partial_x \overline{T^*} \rangle$ [CB14, *Sampe and Xie*, 2010]; nevertheless, we find a negative correlation between $\overline{P}$ and $-\langle [\overline{u}] \partial_x \overline{T^*} \rangle$ everywhere in the EASM domain. Thermal effects by the TP and land-sea contrast result in a negative longitudinal temperature gradient in the EASM region. Convection will tend to smooth out this temperature gradient in the free troposphere, which helps explain the observed negative correlation. The correlation between precipitation and the term $-\langle \overline{v^*[\partial_y T]} \rangle$ varies significantly amongst different models; however, when we only consider $\langle \overline{v^*} \rangle$, correlations increase and the model spread decreases significantly, especially in East China (also see the close coincidence of spatial patterns of precipitation and $\{\overline{v^*}\}$ from observations in Figure 1c), with the exception of two outliers. Finally, the largest spatial correlations are obtained when we consider the combined effect of $\overline{F^{\text{net}}} - \langle \overline{v^*[\partial_y T]} \rangle$. A nonparametric test with bootstrapping techniques shows that the correlation between $\overline{P}$ and $\overline{F^{\text{net}}} - \langle \overline{v^*[\partial_y T]} \rangle$ is significantly larger than the correlation between $\overline{P}$ and $\overline{F^{\text{net}}}$ alone (The null hypothesis in the test is that the mean of the
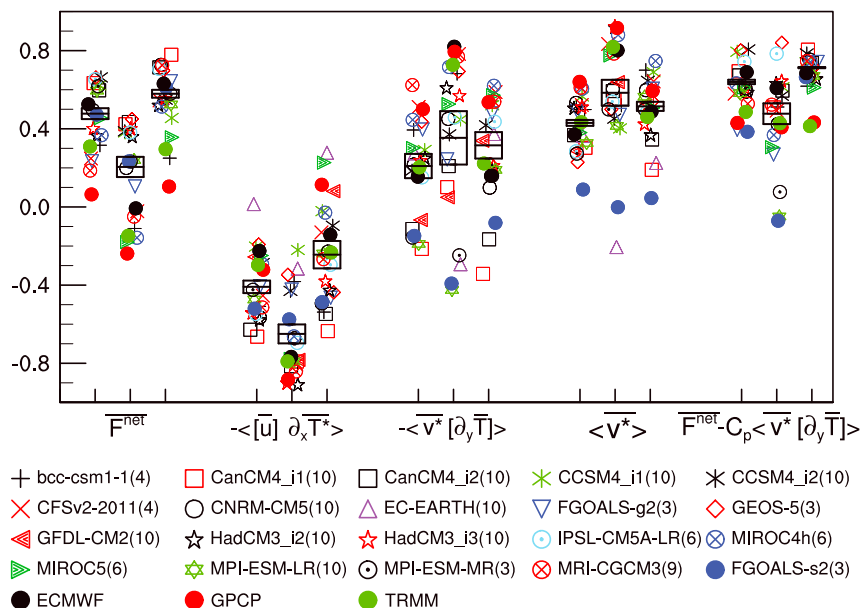
Figure 2. Spatial pattern correlation (centered) between the precipitation over (left in each column) the EASM region, (middle in each column) East China, and (right in each column) the CBP region and the metrics indicated in the diagram. Each metric is summarized by a boxplot, characterized by mean value and standard deviation of correlation (with the exception of FGOALS-s2). The names of the 17 models and three additional experiments with different initialization method are labeled in the legend, with initialization methods (when necessary) labeled with i# and numbers in parentheses indicating the number of ensembles.

two sample pools is the same. For any constructed samples with size larger than 4 out of a total sample pool of size 17 (EC-EARTH and GFDL-CM2 are not included because of incomplete data outputs) with 10,000 random repetitions, the null hypothesis can be rejected at the 0.01 level.) This confirms that in spite of differing simulated precipitation over the EASM region, the underlying dynamics is the same across models and data: the combined positive pattern of the advection of the mean meridional temperature gradient by the stationary eddy meridional velocity, $\langle -\overline{v^*}[\partial_y\overline{T}]\rangle$, and the net energy input into the atmospheric column, $\overline{F^{net}}$, is the most important large-scale factor controlling the spatial distribution of precipitation in the EASM region.

The analysis above suggests that anomalies in the EASM precipitation are strongly correlated with biases in the simulated $\langle\overline{v^*}\rangle$, which is primarily due to topographically-induced stationary waves and the resulting diabatic heating distribution [CB14, *Rodwell and Hoskins*, 2001; *Wu et al.*, 2007; *Park et al.*, 2012]. The reasons of such disparate simulations of $\langle\overline{v^*}\rangle$ remain unclear, but are likely to be affected by the model's resolution and the interaction of the model's physics with the simulated large-scale circulation.

3.2. Rainfall Amount

How can biases in the simulated large-scale dynamics constrain biases in simulated rainfall amounts? The simulated EASM regional precipitation (Figure 3) shows a wide range across the 17 climate models, with most models producing an area average of 4.2–5.0 mm d^{-1}, and minima and maxima ranging between ~3.5 mm d^{-1} (EC-EARTH) and ~6.5 mm d^{-1} (HadCM3). ERA-Interim precipitation is also presented as a reference. It is not unreasonable to expect that models with moist (dry) biases in the global average might have similarly signed biases in precipitating regions (see *Muller and O'Gorman* [2011] for similar arguments on the regional precipitation response to climate change). The spread in the simulated EASM rainfall $\overline{P}$, especially in East China, can in fact be partially explained by the spread in the simulated background global precipitation $[\overline{P}]$ (Figures 3a and 3d). The remaining spread arises, rather than from evaporation $\overline{E}$, from spread in mean moisture flux convergence $\langle\nabla\cdot\overline{\mathbf{v}}\,\overline{q}\rangle$, which is close to the total moisture flux convergence $\langle\nabla\cdot\overline{\mathbf{v}q}\rangle$ because of almost negligible transient term in most climate models. CB14 show that the largest contribution to the vertically integrated moisture convergence comes from the moisture weighted meridional stationary eddy convergence integrated from the surface to 700 mb, i.e., MWC $= -\int_{surf}^{700mb}\overline{q}^d\,\partial_y\overline{v^*}^d\,\mathrm{d}p/g$, where superscript d denotes the decadal climatological average. Figures 3b, 3e, and 3h show that this metric provides a remarkable, albeit not perfect, estimate of the total moisture flux convergence and accounts for the spread across all climate models.
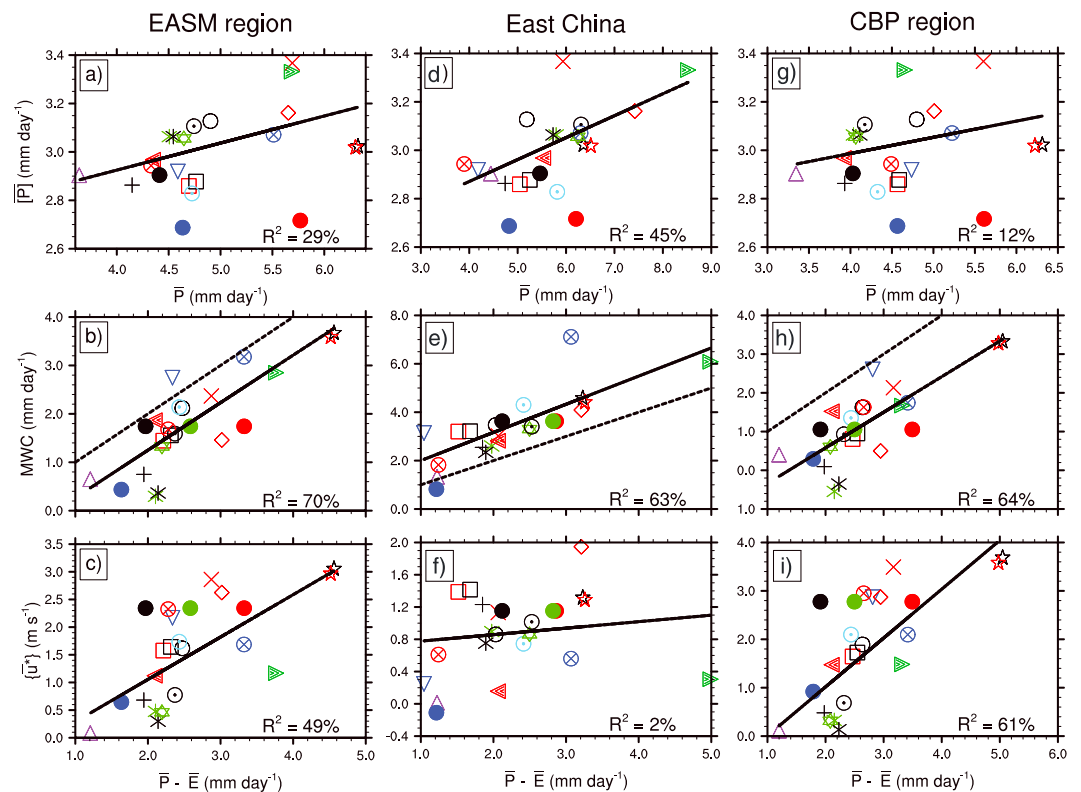
Figure 3. Regression (a, d, and g) between the regional precipitation $\overline{P}$ (x axis) and global precipitation $[\overline{P}]$ (y axis), (b, e, and h) between the estimated moisture flux convergence $\overline{P} - \overline{E}$ (x axis) and normalized MWC $= -\int_{surf}^{700mb} \overline{q}^d \partial_y \overline{v^*}^d\, dp$ (y axis), and (c, f, and i) vertically normalized stationary zonal wind eddy velocity $\{\overline{u^*}\}$ (y axis) over the EASM region in Figures 3a–3c, East China in Figures 3d–3f, and the CBP region in Figures 3g–3i. The coefficient of determination R^2 is calculated based on all models except for FGOALS-s2, which does not satisfy the global P-E budget, excludes ECMWF reanalysis and GPCP and TRMM products and is significant at the 95% level of a two-tailed Student's t test if larger than 21%. The dashed line denotes the one-to-one relationship.

The empirical association of the EASM precipitation and the subtropical westerly jet has been discussed in many studies [e.g., CB14; *Kodama*, 1992; *Sampe and Xie*, 2010]. While several hypotheses have been proposed to explain this association, thermal wind balance suggests a direct link between the intensity and location of the upper tropospheric subtropical westerly jet and the horizontal temperature gradient, which is influenced by the atmospheric diabatic heating [*Zhang et al.*, 2006]. The westerly winds have an equivalent barotropic structure over the EASM region, so we use the vertically normalized zonal eddy velocity $\{\overline{u^*}\} = \frac{1}{(p_{bottom}-p_{top})}\int \overline{u^*}\,dp$ (e.g., Figure 1b, linear contour) as an index of the subtropical westerly jet core. Precipitation amounts are indeed well correlated to $\{\overline{u^*}\}$ in regions of strong meridional temperature gradient, such as the CBP region (Figure 3i). However, no such correlation is observed over East China, where meridional temperature gradients are weak (Figure 3f).

4. Conclusions

CMIP5 simulations of the EASM have been assessed within the MSE and moisture budgets. We have shown that the spatial distribution of the simulated precipitation is strongly correlated to the sum of the net energy input into the atmospheric column and the zonal mean temperature advection by the meridional stationary velocity $\overline{F^{net}} - \langle \overline{v^*}[\partial_y \overline{T}] \rangle$. In terms of rainfall amounts, we find that the wide intermodel spread can be only partly related to the background spread in the globally averaged precipitation (particularly over East China) and is primarily due to disparate simulations of the large-scale circulation as characterized by the lower level meridional stationary wind convergence. In both analyses, the stationary eddy velocity $\langle \overline{v^*} \rangle$ appears to be the most important single metric capturing the intermodel spread. The meridional eddy velocity over the EASM region is primarily due to stationary waves induced by land-sea contrast and the TP (CB14), and their interaction with the resulting diabatic heating, highlighting existing deficiencies in how GCMs represent

moisture-circulation interactions. These conclusions are consistent with those in CB14 and are expected to provide useful constraints for future projection of the EASM and other STCZs.

The EASM rainfall amount is partially affected by the simulated globally averaged precipitation, whose spread should be energetically constrained on annual averages, but might be only loosely constrained over monthly timescales because of atmospheric heat storage. The range in the simulated June and July global precipitation amongst different models is as large as 0.7 mm d^{-1}, which is equivalent to ~18 W m^{-2} difference in atmospheric latent heating. Such spread in latent heating can be examined using observations, such as the Clouds and the Earth's Radiant Energy System-Energy Balanced And Filled together with sensible heat in ERA-Interim and attributed to errors in simulated radiative and/or heat fluxes. This will be explored in future studies.

Analyses similar to those discussed here will be used to investigate future projections on the regional scale. We will specifically explore if the intermodel spread in future EASM changes in response to increasing greenhouse gases will diverge, based on the existing wide spread in the present-day climate simulations. If so, identifying key processes that need to be accurately represented in climate models to better constrain present-day climate, as we do in this study, is the first necessary step to reduce uncertainties in future projections of the EASM and ultimately provide effective guidance to adaptation measures at the regional scale.

References

Adler, R. F., G. J. Huffman, D. T. Bolvin, S. Curtis, and E. J. Nelkin (2000), Tropical rainfall distributions determined using TRMM combined with other satellite and rain gauge information, *J. Appl. Meteorol.*, *39*(12), 2007–2023.

Adler, R. F., J.-J. Wang, G. Gu, and G. J. Huffman (2009), A ten-year tropical rainfall climatology based on a composite of TRMM products, *J. Meteorol. Soc. Jpn.*, *87*, 281–293.

Berrisford, P., P. Kållberg, S. Kobayashi, D. Dee, S. Uppala, A. Simmons, P. Poli, and H. Sato (2011), Atmospheric conservation properties in ERA-Interim, *Q. J. R. Meteorol. Soc.*, *137*(659), 1381–1399.

Bony, S., B. Stevens, I. H. Held, J. F. Mitchell, J.-L. Dufresne, K. A. Emanuel, P. Friedlingstein, S. Griffies, and C. Senior (2013), Carbon dioxide and climate: Perspectives on a scientific assessment, in *Climate Science for Serving Society*, edited by G. R. Asrar and J. W. Hurrell, pp. 391–413, Springer, Dordrecht.

Boos, W. R., and J. V. Hurley (2013), Thermodynamic bias in the multimodel mean boreal summer monsoon, *J. Clim.*, *26*(7), 2279–2287.

Ceppi, P., Y.-T. Hwang, D. M. Frierson, and D. L. Hartmann (2012), Southern Hemisphere jet latitude biases in CMIP5 models linked to shortwave cloud forcing, *Geophys. Res. Lett.*, *39*, L19708, doi:10.1029/2012GL053115.

Chen, H., T. Zhou, R. B. Neale, X. Wu, and G. J. Zhang (2010), Performance of the new NCAR CAM3. 5 in East Asian summer monsoon simulations: Sensitivity to modifications of the convection scheme, *J. Clim.*, *23*(13), 3657–3675.

Chen, J., and S. Bordoni (2014), Orographic effects of the Tibetan Plateau on the East Asian summer monsoon: An energetic perspective, *J. Clim.*, doi:10.1175/JCLI-D-13-00479.1, in press.

Dee, D., et al. (2011), The ERA-Interim reanalysis: Configuration and performance of the data assimilation system, *Q. J. R. Meteorol. Soc.*, *137*(656), 553–597, doi:10.1002/qj.828.

Huang, D.-Q., J. Zhu, Y.-C. Zhang, and A.-N. Huang (2013), Uncertainties on the simulated summer precipitation over Eastern China from the CMIP5 models, *J. Geophys. Res. Atmos.*, *118*, 9035–9047, doi:10.1002/jgrd.50695.

Kodama, Y.-M. (1992), Large-scale common features of subtropical precipitation zones (the Baiu Frontal Zone, the SPCZ and the SACZ) part I: Characteristics of subtropical frontal zones, *J. Meteorol. Soc. Jpn.*, *70*, 813–836.

Meehl, G. A., et al. (2007), Global climate projections, in *Climate Change 2007: The Physical Science Basis. Contribution of Working Group I to the Fourth Assessment Report of the Intergovernmental Panel on Climate Change*, edited by S. Solomon et al., pp. 996, Cambridge Univ. Press, Cambridge, U.K., and New York.

Meehl, G. A., et al. (2009), Decadal prediction: Can it be skillful?, *Bull. Am. Meteorol. Soc.*, *90*(10), 1467–1485.

Muller, C., and P. O'Gorman (2011), An energetic perspective on the regional response of precipitation to climate change, *Nat. Clim. Change*, *1*(5), 266–271.

O'Gorman, P. A., R. P. Allan, M. P. Byrne, and M. Previdi (2012), Energetic constraints on precipitation under climate change, *Surv. Geophys.*, *33*(3-4), 585–608.

Park, H.-S., J. Chiang, and S. Bordoni (2012), Mechanical impact of the Tibetan Plateau on the seasonal evolution of the South Asian monsoon, *J. Clim.*, *25*, 2394–2407.

Rodwell, M., and B. Hoskins (2001), Subtropical anticyclones and summer monsoons, *J. Clim.*, *14*(15), 3192–3211.

Sampe, T., and S. Xie (2010), Large-scale dynamics of the Meiyu-Baiu rainband: Environmental Forcing by the westerly jet, *J. Clim.*, *23*(1), 113–134.

Song, F., and T. Zhou (2013), Inter-annual variability of east asian summer monsoon simulated by CMIP3 and CMIP5 AGCMs: Skill dependence on Indian Ocean-western Pacific anticyclone teleconnection, *J. Clim.*, *27*, 1679–1697, doi:10.1175/JCLI-D-13-00248.1.

Song, F., T. Zhou, and Y. Qian (2013), Responses of East Asian summer monsoon to natural and anthropogenic forcings in the 17 latest CMIP5 models, *Geophys. Res. Lett.*, doi:10.1002/2013GL058705.

Sperber, K. R., H. Annamalai, I.-S. Kang, A. Kitoh, A. Moise, A. Turner, B. Wang, and T. Zhou (2012), The Asian summer monsoon: An intercomparison of CMIP5 vs. CMIP3 simulations of the late 20th century, *Clim. Dyn.*, *41*, 2711–2744.

Stevens, B., and S. Bony (2013), What are climate models missing?, *Science*, *340*(6136), 1053–1054.

Taylor, K. E., R. J. Stouffer, and G. A. Meehl (2012), An overview of CMIP5 and the experiment design, *Bull. Am. Meteorol. Soc.*, *93*(4), 485–498.

Teixeira, J., D. Waliser, R. Ferraro, P. Gleckler, and G. Potter (2011), Satellite observations for CMIP5 simulations. CLIVAR Exchanges No. 56, Vol. 16, No.2.

Wu, G., et al. (2007), The influence of mechanical and thermal forcing by the Tibetan Plateau on Asian climate, *J. Hydrometeorol.*, *8*, 770–789.

Zhang, Y., X. Kuang, W. Guo, and T. Zhou (2006), Seasonal evolution of the upper-tropospheric westerly jet core over East Asia, *Geophys. Res. Lett.*, *33*(11), L11708, doi:10.1029/2006GL026377.

Zhou, T., et al. (2009), Why the western Pacific subtropical high has extended westward since the late 1970s, *J. Clim.*, *22*(8), 2199–2215.